Zero-Level Control Design in AC Microgrids: A Robust Multivariable Approach

Ali Rafiee, Yazdan Batmani, Ali Mehrizi-Sani, *Senior Member, IEEE*, Toshiji Kato, *Life Senior Member, IEEE*, and Hassan Bevrani, *Fellow, IEEE*

***Abstract*—In this article, a multi-input multioutput robust proportional–integral (PI) controller is designed for zero-level control of ac microgrids. The study system is a voltage-sourced converter connected to the rest of the microgrid through a distribution line and an ac output filter. The design procedure of the proposed high-gain PI controller is independent from the state matrix of the distributed energy resources. Severe local load changes are considered as the system unknown disturbances. It is proved that the closed-loop system behaves like a first-order system with stable internal dynamics. As the bandwidth of the suggested zero-level control can be systematically adjusted, it can properly operate in both high and medium frequencies without considerable fluctuations and overshoots at the output. It is also shown that circulating currents, which can cause overcurrent conditions in power electronic devices and damage dc-link capacitors, are limited without using any limiters. By considering some realistic scenarios and through time-domain simulations in MATLAB/Simulink and a supporting experimental test, it is shown that the proposed strategy can successfully attenuate adverse effects of unknown disturbances on the load voltage of islanded microgrids.**

***Index Terms*—High-gain proportional–integral (PI) controller, microgrid, multi-input multioutput (MIMO) control, voltage control.**

I. Introduction

MICROGRIDS, the building blocks of the smart grid, are micronetworks composed of distributed energy resources (DERs), energy storage systems, distribution lines, and consumer loads that operate autonomously or in connection with the main utility grid. To provide frequency and voltage stability, main grid synchronization, cost-effective energy management, active/reactive power control sharing among DERs, and upstream-connected networks, a hierarchical control framework with different control objectives in different time scale and functionalities has been established [1], [2]. Voltage and frequency stability for microgrids in the grid-connected mode are dictated by the main grid, and following islanding, an effective control strategy should establish reliable operating conditions [3]. In the hierarchical control structure, the primary control level operates at the fastest time constant (milliseconds to seconds) to stabilize the voltage and frequency, to provide plug-and-play possibility for DERs, to share the active and reactive powers among DERs, and to mitigate circulating currents that can cause the overcurrent phenomenon in power electronic devices [4]. As shown in Fig. 1, the primary control level establishes the architecture of the main control loops, including the independent inner current and voltage loops (also known as zero-level control) and the outer droop loops. The droop controllers compare the active power and reactive power with their command values and provide the frequency set point and voltage reference. The inner control loop is established for voltage tracking with zero steady-state errors using the synchronous *dq* reference frame [4], [5]. The bandwidth (BW) of zero-level control loops should be higher than that of outer loops. The voltage control loop regulates capacitor voltage and provides references for the inner current control loop. For these applications, the proportional–integral (PI) controllers with feedback and feedforward terms and a decoupling component have been widely utilized in the reference frame *dq* [4]. These controllers, however, are susceptible to high overshoots, and they are sensitive to parameter fluctuations and system nonlinearity. Therefore, these controllers are unable to ensure the accurate transient power sharing [6]. Furthermore, the changes in the output power of the inverter in response to disturbances, caused by load changes, are associated with high-frequency fluctuations; and thus, the outer control layer must be equipped with a low-pass filter with a cutoff frequency of ω_c, which is typically tuned a decade below the nominal frequency [7].

As stated, although the zero-level control has a sufficient BW, the overall BW of the primary control level is dictated by the low-pass filter's cutoff frequency. Hence, the higher control layers, such as the secondary control level, must have BWs lower than the BW of the primary control level. From a practical point of view, the secondary control with low BW may be affected by communication network uncertainty and cyberattacks [8]. Consequently, utilizing a fast and robust control structure in the primary control level is one of the essential requirements for the microgrid control reliability, and many techniques have been proposed to improve primary control BWs. Among these methods, model predictive control (MPC), robust control, and

Manuscript received 6 January 2023; revised 20 March 2023; accepted 15 April 2023. Date of publication 21 April 2023; date of current version 19 May 2023. Recommended for publication by Associate Editor F. D. Freijedo. *(Corresponding author: Yazdan Batmani.)*

Ali Rafiee, Yazdan Batmani, and Hassan Bevrani are with the Department of Electrical Engineering, University of Kurdistan, Sanandaj 66177-15175, Iran (e-mail: ali.rafiee@uok.ac.ir; y.batmani@uok.ac.ir; h.bevrani@uok.ac.ir).

Ali Mehrizi-Sani is with the Bradley Department of Electrical and Computer Engineering, Virginia Tech, Blacksburg, VA 24061 USA (e-mail: mehrizi@vt.edu).

Toshiji Kato is with the Department of Electrical Engineering, Doshisha University, Kyoto 602-8580, Japan (e-mail: tkato@mail.doshisha.ac.jp).

Color versions of one or more figures in this article are available at https://doi.org/10.1109/TPEL.2023.3268865.

Digital Object Identifier 10.1109/TPEL.2023.3268865

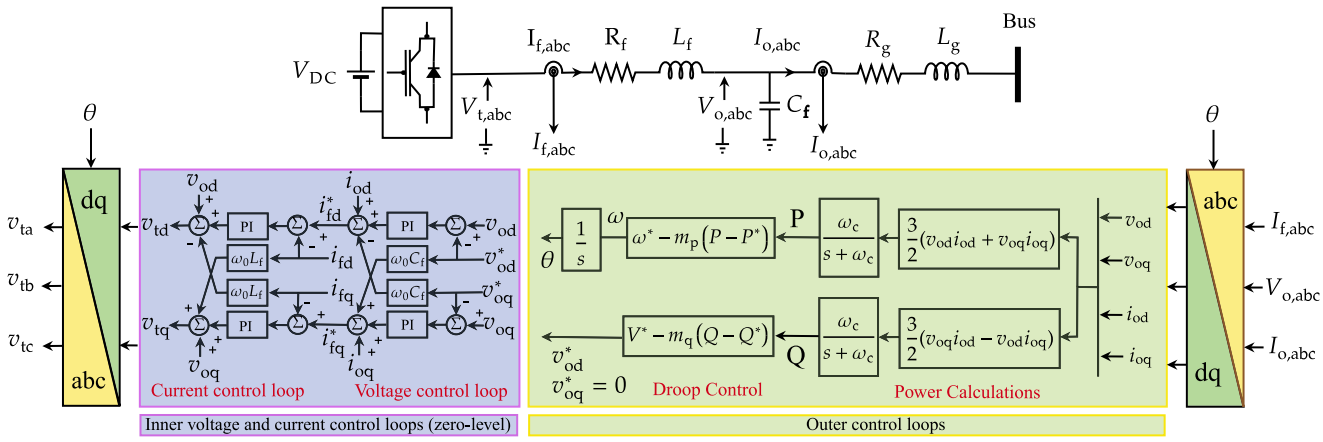

Fig. 1. Electrical configuration and primary control level of an electronically interfaced DER.

optimal control are more common [6], [9], [10]. In [8], [11], [12], and [13], the basic configurations of the MPC, finite control set MPC, and continuous control set MPC were used to improve the zero-level control performance. Although the MPC approach is effective, there are still challenges in its industrial applications. For example, in order to commence control of switch converters, the underlying MPC algorithm must solve an optimization problem, which is time-consuming, especially if a large prediction horizon is selected to achieve satisfactory results. Besides, other challenges, such as variable switching frequencies and wide harmonic spectrum, should be taken into account [14]. For the primary control-level design, robust techniques, such as H_2, H_∞, mix H_2/H_∞, and an iterative μ-based solution, were investigated [10], [15], [16], [17]. In general, when classical robust control methods are used in multivariable systems, setting control specifications is a challenge [18], [19]. Furthermore, in designing an H_∞ controller, the controller is usually high order [20]. In recent works, the development of the primary control loops is based on the state/output feedback methods [9], [21], [22]. These control strategies lack sufficient robustness against changes in the system dynamics. They need to be equipped with integrators in order to achieve reference tracking with zero steady-state error [10], [15], [22].

In the aforementioned approaches, the active and reactive power filters are removed by designing a zero-level controller with a broad BW in their control structure. For instance, a super-high-BW inner control was introduced in [1] and [6]. In [9], an inner controller with a BW about 12.5 times wider than that of the conventional inner control was suggested. Although the tracking objective can be achieved by increasing the BW of the closed-loop system, large control signals are needed that can cause saturation in the actuators.

While using proportional–integral–derivative controllers in the zero-level control of inverter-based microgrids raises some concerns, they still play an important role because of their simple structure [23]. In this article, a high-gain robust multi-input multioutput (MIMO) PI controller is proposed to design inner-loop compensators in the zero-level control of islanded microgrids. The obtained closed-loop system is robust against uncertainty and disturbances. To design the controller, the DERs are modeled as MIMO systems with two control inputs (the modulating signals in the *dq* framework) and two outputs [the amplitudes of the voltages in the point of common coupling (PCC) in the *dq* frame]. Then, the parameters of the proposed high-gain PI (HGPI) controller are tuned based on the first Markov parameter of the microgrid that can be identified in its state-space representation. Since the first Markov parameter is the multiplication of the system input and output matrices [24], the designed MIMO controller is independent of the state matrix of the system and guarantees the robust stability and performance of the closed-loop system. Simulation and experimental results show that the proposed controller successfully regulates the microgrid output voltages even in the presence of severe uncertainties. In summary, the main advantages of the proposed controller are as follows.

1) A stable first-order transfer function is obtained for the closed-loop system where the system internal dynamics is guaranteed to be stable. Therefore, the structure of the control system is simple to be analyzed.
2) Since the closed-loop system is first-order in which the output voltage follows the reference input without any steady-state error, there are no considerable fluctuations or overshoots at the output. Therefore, the output power is directly measured without employing low-pass filters. In contrast to the other approaches, the proposed method can properly operate in both high and medium frequencies as there are no low-pass filters.
3) Circulating currents, which can cause overcurrent conditions in power electronic devices and damage dc-link capacitors, are directly limited without needing any limiters.
4) The suggested controller satisfies the inner-loop control requirements in both grid-connected and islanded operation modes of DERs, and also offers plug-and-play capability for DERs.
5) Concerning some limited knowledge of the system model, the proposed high-gain MIMO PI controller is robust against parametric uncertainty.

The rest of this article is organized as follows. The design procedure of the high-gain robust MIMO PI controller is presented in Section II. In Section III, the studied microgrid is

presented and equipped with the proposed controller. Section IV presents the simulation results of applying the controller to the microgrid. Experimental results are presented in Section V. Finally, Section VI concludes this article.

II. MIMO PI Controller Design

Consider the following dynamical system:

$$\dot{\mathbf{x}}(t) = \mathbf{A}\mathbf{x}(t) + \mathbf{B}\mathbf{u}(t)$$
$$\mathbf{y}(t) = \mathbf{C}\mathbf{x}(t) \tag{1}$$

where $\mathbf{x}(t) \in \mathbb{R}^n$ is the system state; $\mathbf{u}(t) \in \mathbb{R}^m$ is the control input; $\mathbf{y}(t) \in \mathbb{R}^q$ is the system output; and $\mathbf{A} \in \mathbb{R}^{n\times n}$, $\mathbf{B} \in \mathbb{R}^{n\times m}$, and $\mathbf{C} \in \mathbb{R}^{q\times n}$ are three unknown matrices. Here, $\mathbb{R}^n$ is the Euclidean space of all n-dimensional real vectors. It is assumed that the system $(\mathbf{A}, \mathbf{B}, \mathbf{C})$ is controllable and observable. Assume further that the state-space representation (1) is a square MIMO one, i.e., $m = q$.

Definition 1: The Markov parameter sequence of (1) is shown with $\{h(i)\}$ $(i = 0, 1, \ldots)$ and defined as $\{\mathbf{0}_{q\times n}, \mathbf{CB}, \mathbf{CAB}, \ldots, \mathbf{CA}^{i-1}\mathbf{B}, \cdots\}$ [24].

The problem is to design a robust output feedback controller such that the closed-loop system is stable and $\mathbf{y}(t)$ asymptotically tracks its desired trajectory. Following the approach presented in [25] and [26], this problem can be solved by designing a high-gain MIMO PI controller if the first Markov parameter of the state-space representation (1) is full rank. Since the studied microgrid does not satisfy this condition, however, an extension of the method should be utilized to achieve the control objectives by introducing extra output measurements [25], [26]. Due to the controllability and observability of $(\mathbf{A}, \mathbf{B}, \mathbf{C})$, there exists a similarity transformation $\begin{bmatrix}\mathbf{x_1^T}(\mathbf{t}) & \mathbf{x}_2^{\mathrm{T}}(t)\end{bmatrix}^{\mathrm{T}} = \mathbf{T}\mathbf{x}(t)$ such that

$$\begin{bmatrix}\dot{\mathbf{x}}_1(t)\\ \dot{\mathbf{x}}_2(t)\end{bmatrix} = \begin{bmatrix}\mathbf{A_{11}} & \mathbf{A}_{12}\\ \mathbf{A}_{21} & \mathbf{A}_{22}\end{bmatrix}\begin{bmatrix}\mathbf{x_1(t)}\\ \mathbf{x}_2(t)\end{bmatrix} + \begin{bmatrix}\mathbf{0}\\ \mathbf{B}_2\end{bmatrix}\mathbf{u}(t) + \begin{bmatrix}\mathbf{D_1}\\ \mathbf{0}\end{bmatrix}\mathbf{d}(t)$$
$$\mathbf{y}(t) = \begin{bmatrix}\mathbf{C_1} & \mathbf{C}_2\end{bmatrix}\begin{bmatrix}\mathbf{x_1(t)}\\ \mathbf{x}_2(t)\end{bmatrix} \tag{2}$$

where $\mathbf{x}_1(t) \in \mathbb{R}^{(n-m)}$, $\mathbf{x}_2(t) \in \mathbb{R}^m$, $\mathbf{d}(t)$ is the external disturbance, and the other matrices ($\mathbf{A}_{ij}$ $(i, j = 1, 2)$, $\mathbf{B}_2$, $\mathbf{D}_1$, $\mathbf{C}_1$, and $\mathbf{C}_2$) are constant with appropriate dimensions. It should be mentioned that $\mathbf{B}_2$ is a nonsingular matrix [26]. When $\mathbf{CB} = \mathbf{C}_2\mathbf{B}_2$ is not full rank, a new output measurement is defined as follows [26]:

$$\begin{aligned}\mathbf{w}(t) &= \mathbf{y}(t) + \mathbf{M}\dot{x}_1(t)\\ &= \begin{bmatrix}\mathbf{C_1} + \mathbf{MA_{11}} & \mathbf{C}_2 + \mathbf{MA}_{12}\end{bmatrix}\begin{bmatrix}\mathbf{x_1(t)}\\ \mathbf{x}_2(t)\end{bmatrix}\\ &= \begin{bmatrix}\mathbf{F_1} & \mathbf{F}_2\end{bmatrix}\begin{bmatrix}\mathbf{x_1(t)}\\ \mathbf{x}_2(t)\end{bmatrix}\end{aligned} \tag{3}$$

where $\mathbf{M}$ is called the measurement matrix that must be selected such that $\mathbf{F}_2\mathbf{B}_2$ is full rank. By designing a proper controller such that the closed-loop system is asymptotically stable and

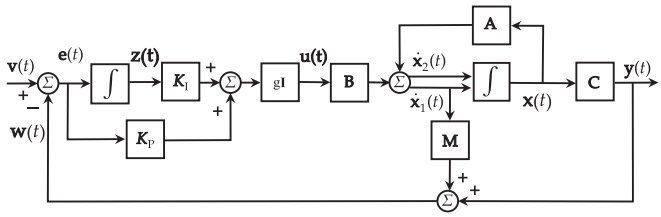

Fig. 2. General structure of the closed-loop system under the high-gain MIMO PI controller.

$\mathbf{y}(t)$ tracks its desired trajectory $\mathbf{v}(t)$, the steady-state values of $\mathbf{y}(t)$ and $\mathbf{w}(t)$ are the same since, when t tends to infinity, $\dot{\mathbf{x}}_1(t)$ tends to zero. One of the control objectives is to eliminate the steady-state tracking error $\mathbf{v}(t) - \mathbf{y}(t)$. In the following, this goal is attained by forcing $\mathbf{e}(t) = \mathbf{v}(t) - \mathbf{w}(t)$ to set to zero. An HGPI controller makes it possible to not only stabilize the closed-loop system but also to achieve the control performance objectives, including the desired inputs tracking. The structure of this controller is given as follows [26]:

$$\mathbf{u}(t) = g\left(\mathbf{K}_{\mathrm{P}}\mathbf{e}(t) + \mathbf{K}_{\mathrm{I}}\mathbf{z}(t)\right) \tag{4}$$

where g is a scalar gain; $\mathbf{K}_{\mathrm{P}}$ and $\mathbf{K}_{\mathrm{I}}$ are the controller gain matrices; and $\mathbf{z}(t)$ is the time integral of error $\mathbf{e}(t)$. The block diagram of the system under the utilized HGPI controller is shown in Fig. 2. Using $\mathbf{e}(t)$ and (3), we have

$$\dot{\mathbf{z}}(t) = \mathbf{e}(t) = \mathbf{v}(t) - \mathbf{w}(t) = \mathbf{v}(t) - \mathbf{F}_1\mathbf{x}_1(t) - \mathbf{F}_2\mathbf{x}_2(t). \tag{5}$$

Therefore, the state and output equations of the closed-loop system and its corresponding transfer function matrix, shown with $\mathbf{G}(s)$, can be represented by (6) and (7) shown at the bottom of the next page, respectively

By defining

$$\mathbf{\Gamma}_s(s) = \mathbf{C}_0(s\mathbf{I}_m - \mathbf{A}_0)^{-1}\mathbf{B}_0 \tag{8}$$
$$\mathbf{\Gamma}_f(s) = \mathbf{C}_2(s\mathbf{I}_{(m-n)} - g\mathbf{A}_4)^{-1}g\mathbf{B}_2\mathbf{K}_P \tag{9}$$
$$\mathbf{A}_0 = \begin{bmatrix}-\mathbf{K}_P^{-1}\mathbf{K}_I & \mathbf{0}\\ \mathbf{A}_{12}\mathbf{F}_2^{-1}\mathbf{K}_P^{-1}\mathbf{K}_I & \mathbf{A}_{11} - \mathbf{A}_{12}\mathbf{F}_2^{-1}\mathbf{F}_1\end{bmatrix} \tag{10}$$
$$\mathbf{B}_0 = \begin{bmatrix}\mathbf{0} & \mathbf{A}_{12}\mathbf{F}_2^{-1}\end{bmatrix}^{\mathrm{T}} \tag{11}$$
$$\mathbf{C}_0 = \begin{bmatrix}\mathbf{C_2F_2^{-1}K_P^{-1}K_I} & \mathbf{C}_1 - \mathbf{C}_2\mathbf{F}_2^{-1}\mathbf{F}_1\end{bmatrix} \tag{12}$$
$$\mathbf{A}_4 = -\mathbf{B}_2\mathbf{K}_P\mathbf{F}_2 \tag{13}$$

it is possible to show that $\mathbf{\Gamma}(s) = \mathbf{\Gamma}_s(s) + \mathbf{\Gamma}_f(s)$ equals the second matrix in the right hand side of (7) when g tends to infinity [26]. $\mathbf{\Gamma}_s(s)$ and $\mathbf{\Gamma}_f(s)$ are "slow" and "fast" asymptotic transfer functions since they contain only the slow and fast modes. The poles of $\mathbf{\Gamma}_s(s)$ are found from $|s\mathbf{I}_m - \mathbf{A}_0| = 0$; and therefore, the slow modes of the closed-loop system are not directly affected by g. Since $\mathbf{A}_0$ is a block lower triangular matrix, the slow poles can be categorized into two different groups. The first group is the poles related to the solutions of $|s\mathbf{I}_m + \mathbf{K}_P^{-1}\mathbf{K}_I| = 0$ that can be stabilized by selecting $\mathbf{K}_{\mathrm{I}} = \alpha\mathbf{K}_{\mathrm{P}}$ where α is an arbitrary positive constant. The

Algorithm 1: High-Gain Robust MIMO PI Controller.

- *Step 1.* Select the measurement matrix $\mathbf{M}$ such that $\mathbf{F}_2$ is full rank and the eigenvalues of $\mathbf{A}_{11}-\mathbf{A}_{12}\mathbf{F}_2^{-1}\mathbf{F}_1$ are placed in the left-half plane.
- *Step 2.* Select the positive values for $\sigma_1,\ldots,\sigma_m$ and construct $\mathbf{\Sigma}=\mathbf{diag}\{\sigma_1,\ldots,\sigma_m\}$.
- *Step 3.* Set the proportional gain $\mathbf{K}_P=(\mathbf{F}_2\mathbf{B}_2)^{-1}\mathbf{\Sigma}$.
- *Step 4.* Select $\alpha>0$ and calculate $\mathbf{K}_I=\alpha\mathbf{K}_P$.
- *Step 5.* Select a large positive value for the gain g.

second group of the slow dynamics is the solutions of $|s\mathbf{I}_m-\mathbf{A}_{11}+\mathbf{A}_{12}\mathbf{F}_2^{-1}\mathbf{F}_1|=0$. These poles are also the zeros of the system and usually can decrease the speed of the closed-loop system response. The poles related to the fast dynamics (roots of $|s\mathbf{I}_{(m-n)}-g\mathbf{A}_4|$) are controllable and observable. These poles are direct functions of g [26].

Design of the tracking controller requires the selection of the measurement matrix $\mathbf{M}$ and the control law matrices $\mathbf{K}_P$ and $\mathbf{K}_I$. In addition, achieving decoupling requires that the asymptotic transfer functions (11) and (12) be diagonal, which are satisfied if $\mathbf{M}$ is chosen so that $\mathbf{F}_2$ is not rank deficient and $\mathbf{F}_2\mathbf{B}_2$ has full rank; and all of the closed-loop poles lie in the open left half of the complex plane [26]. $\mathbf{\Gamma}_f(s)$ in (9) is diagonal, if

$$\mathbf{F}_2\mathbf{B}_2\mathbf{K}_P=(\mathbf{C}_2+\mathbf{M}\mathbf{A}_{12})\mathbf{B}_2\mathbf{K}_P=\mathbf{\Sigma}=\mathbf{diag}\{\sigma_1,\ldots,\sigma_n\}$$

where $\sigma_n>0$. Then, the fast eigenvalues are $\{-\sigma_1\, g,\ldots,-\sigma_n g\}$. A synthesis procedure for selecting the measurement matrix is to form $\mathbf{F}_2=\mathbf{C}_2+\mathbf{M}\mathbf{A}_{12}$ and to select the most sparse matrix $\mathbf{M}$ that produces a matrix $\mathbf{F}_2$ of full rank. Simultaneously, the matrix product $\mathbf{C}_2\mathbf{F}_2^{-1}$ must be made diagonal. The following algorithm summarizes the design procedure of the high-gain robust MIMO PI controller. More details can be found in [26].

III. Microgrid Controller Synthesis

The single line diagram of the inverter-based DER connected to the rest of the microgrid at the PCC is shown in Fig. 1. Since the rest of the microgrid's dynamic is uncertain, the currents drawn by the system at the PCC are considered as externally bounded and measurable disturbances. Thus, the following differential equations are obtained to describe the current and voltage dynamics:

$$L_{\rm f}\frac{{\rm d}\mathbf{i}_{f,abc}}{{\rm d}t}=\mathbf{v}_{\rm t,abc}-R_{\rm f}\mathbf{i}_{\rm f,abc}-\mathbf{v}_{\rm o,abc}$$
$$C_{\rm f}\frac{{\rm d}\mathbf{v}_{\rm o,abc}}{{\rm d}t}=\mathbf{i}_{\rm f,abc}-\mathbf{i}_{\rm o,abc}. \tag{14}$$

Each three-phase variable $\mathbf{x}_{\rm abc}$ in (14) can be transferred to a stationary $\alpha\beta$ reference frame under balanced conditions by performing the following abc to $\alpha\beta$ transformation [27]:

$$x_{\alpha\beta}=x_{\rm a}e^{j0}+x_{\rm b}e^{j\frac{2\pi}{3}}+x_{\rm c}e^{j\frac{4\pi}{3}} \tag{15}$$

where $x_{\alpha\beta}=x_\alpha+jx_\beta$. Hence, the system's model in the $\alpha\beta$ frame is given as follows:

$$L_{\rm f}\frac{{\rm d}\mathbf{i}_{f,\alpha\beta}}{{\rm d}t}=\mathbf{v}_{\rm t,\alpha\beta}-R_{\rm f}\mathbf{i}_{\rm f,\alpha\beta}-\mathbf{v}_{\rm o,\alpha\beta}$$
$$C_{\rm f}\frac{{\rm d}\mathbf{v}_{\rm o,\alpha\beta}}{{\rm d}t}=\mathbf{i}_{\rm f,\alpha\beta}-\mathbf{i}_{\rm o,\alpha\beta}. \tag{16}$$

The $\alpha\beta$ to the dq-frame transformation is defined by

$$x_{\alpha\beta}=X_{\rm dq}e^{j\theta}=(X_{\rm d}+jX_{\rm q})e^{j\theta} \tag{17}$$

where $\theta(t)=\int_0^t\omega(\tau){\rm d}\tau+\theta_0$ is the transformation angle. Therefore, for the system's nominal frequency $\omega_0>0$, the transformation angle is $\theta(t)=\omega_0 t+\theta_0$. Substituting the $\alpha\beta$ variables from (17) into (16) leads to

$$L_{\rm f}\left(\frac{{\rm d}\mathbf{i}_{f,dq}}{dt}+j\omega_0\mathbf{i}_{\rm f,dq}\right)=\mathbf{v}_{\rm t,dq}-R_{\rm f}\mathbf{i}_{\rm f,dq}-\mathbf{v}_{\rm o,dq}$$
$$C_{\rm f}\left(\frac{{\rm d}\mathbf{v}_{\rm o,dq}}{dt}+j\omega_0\mathbf{v}_{o,dq}\right)=\mathbf{i}_{\rm f,dq}-\mathbf{i}_{\rm o,dq} \tag{18}$$

where each equation in (18) can be represented in terms of the d- and q-axis components of the state variables by two scalar equations. The resulting standard form for the set of scalar equations derived from (18) is given as follows [11], [15]:

$$\begin{bmatrix}\dot v_{\rm od}(t)\\ \dot v_{\rm oq}(t)\\ \dot i_{\rm fd}(t)\\ \dot i_{\rm fq}(t)\end{bmatrix}=\left[\begin{array}{cc:cc}0&\omega_0&\frac{1}{C_{\rm f}}&0\\ -\omega_0&0&0&\frac{1}{C_{\rm f}}\\ \hdashline -\frac{1}{L_{\rm f}}&0&-\frac{R_{\rm f}}{L_{\rm f}}&\omega_0\\ 0&-\frac{1}{L_{\rm f}}&-\omega_0&-\frac{R_{\rm f}}{L_{\rm f}}\end{array}\right]\begin{bmatrix}v_{\rm od}(t)\\ v_{\rm oq}(t)\\ i_{\rm fd}(t)\\ i_{\rm fq}(t)\end{bmatrix}$$

$$\begin{bmatrix}\dot{\mathbf{z}}(t)\\ \dot{\mathbf{x}}_1(t)\\ \dot{\mathbf{x}}_2(t)\end{bmatrix}=\begin{bmatrix}\mathbf{0}_{\mathbf{m}\times\mathbf{m}}&-\mathbf{F}_1&-\mathbf{F}_2\\ \mathbf{0}_{(n-m)\times m}&\mathbf{A}_{11}&\mathbf{A}_{12}\\ g\mathbf{B}_2\mathbf{K}_I&\mathbf{A}_{21}-g\mathbf{B}_2\mathbf{K}_P\mathbf{F}_1&\mathbf{A}_{22}-g\mathbf{B}_2\mathbf{K}_P\mathbf{F}_2\end{bmatrix}\begin{bmatrix}\mathbf{z(t)}\\ \mathbf{x}_1(t)\\ \mathbf{x}_2(t)\end{bmatrix}+\begin{bmatrix}\mathbf{I_m}\\ \mathbf{0}_{(n-m)\times m}\\ g\mathbf{B}_2\mathbf{K}_P\end{bmatrix}\mathbf{v}(t)$$

$$\mathbf{y}(t)=\begin{bmatrix}\mathbf{0_{q\times m}}&\mathbf{C}_1&\mathbf{C}_2\end{bmatrix}\begin{bmatrix}\mathbf{z(t)}\\ \mathbf{x}_1(t)\\ \mathbf{x}_2(t)\end{bmatrix} \tag{6}$$

$$\mathbf{G}(s)=\begin{bmatrix}\mathbf{0_{q\times m}}&\mathbf{C}_1&\mathbf{C}_2\end{bmatrix}\begin{bmatrix}s\mathbf{I}_m&\mathbf{F}_1&\mathbf{F}_2\\ \mathbf{0}_{(n-m)\times m}&s\mathbf{I}_{(m-n)}-\mathbf{A}_{11}&-\mathbf{A}_{12}\\ -g\mathbf{B}_2\mathbf{K}_I&-\mathbf{A}_{21}+g\mathbf{B}_2\mathbf{K}_P\mathbf{F}_1&s\mathbf{I}_m-\mathbf{A}_{22}+g\mathbf{B}_2\mathbf{K}_P\mathbf{F}_2\end{bmatrix}^{-1}\begin{bmatrix}\mathbf{I_m}\\ \mathbf{0}_{(n-m)\times m}\\ g\mathbf{B}_2\mathbf{K}_P\end{bmatrix}. \tag{7}$$

$$+\begin{bmatrix} 0 & 0 \\ 0 & 0 \\ \hdashline \frac{1}{L_\mathrm{f}} & 0 \\ 0 & \frac{1}{L_\mathrm{f}} \end{bmatrix}\begin{bmatrix} v_{\mathrm{td}}(t) \\ v_{\mathrm{tq}}(t) \end{bmatrix}+\begin{bmatrix} -\frac{1}{C_\mathrm{f}} & 0 \\ 0 & -\frac{1}{C_\mathrm{f}} \\ \hdashline 0 & 0 \\ 0 & 0 \end{bmatrix}\begin{bmatrix} i_{\mathrm{od}}(t) \\ i_{\mathrm{oq}}(t) \end{bmatrix}$$

$$\begin{bmatrix} v_{\mathrm{od}}(t) \\ v_{\mathrm{oq}}(t) \end{bmatrix}=\left[\begin{array}{cc:cc} 1 & 0 & 0 & 0 \\ 0 & 1 & 0 & 0 \end{array}\right]\begin{bmatrix} v_{\mathrm{od}}(t) \\ v_{\mathrm{oq}}(t) \\ \hdashline i_{\mathrm{fd}}(t) \\ i_{\mathrm{fq}}(t) \end{bmatrix}, \tag{19}$$

where $v_{\mathrm{od}}(t)$ and $v_{\mathrm{oq}}(t)$ are the dq components of the PCC voltage; $i_{\mathrm{fd}}(t)$ and $i_{\mathrm{fq}}(t)$ are the dq components of the inverter output current; $v_{\mathrm{td}}(t)$ and $v_{\mathrm{tq}}(t)$ are the dq components of the ac-side terminal voltage of the inverter linked to the modulating signal in the dq framework; $i_{\mathrm{od}}(t)$ and $i_{\mathrm{oq}}(t)$ are the dq components of the output current at the PCC; L_f, R_f, and C_f are the filter inductor, resistance, and capacitor, respectively. By defining $\mathbf{x}_1(t)=\begin{bmatrix} v_{\mathrm{od}}(t) & v_{\mathrm{oq}}(t) \end{bmatrix}^T$, $\mathbf{x}_2(t)=\begin{bmatrix} i_{\mathrm{fd}}(t) & i_{\mathrm{fq}}(t) \end{bmatrix}^T$, $\mathbf{x}(t)=\begin{bmatrix} \mathbf{x}_1^{\mathrm{T}}(\mathbf{t}) & \mathbf{x}_2^{\mathrm{T}}(t) \end{bmatrix}^{\mathrm{T}}$, $\mathbf{u}(t)=\begin{bmatrix} v_{\mathrm{td}}(t) & v_{\mathrm{tq}}(t) \end{bmatrix}^T$, $\mathbf{y}(t)=\begin{bmatrix} v_{\mathrm{od}}(t) & v_{\mathrm{oq}}(t) \end{bmatrix}^T$, and the external disturbance $\mathbf{d}(t)=\begin{bmatrix} i_{\mathrm{od}}(t) & i_{\mathrm{oq}}(t) \end{bmatrix}$, the state-space representation of the system is expressed in the standard form (2).

Prior to the design of the controller, a brief analysis of the open-loop system is beneficial. Using (19) as a MIMO system with two inputs and two outputs, the matrix transfer function of the system is $\mathbf{y}(s)=\mathbf{G}(s)\mathbf{u}(s)$, where $\mathbf{G}(s)=\mathbf{C}(s\mathbf{I}-\mathbf{A})^{-1}\mathbf{B}$. According to the inverse of a partitioned matrix lemma [28] and after some simplifications and by defining $\mathbf{X}^{-1}=(\mathbf{A}_{22}-\mathbf{A}_{21}\mathbf{A}_{11}^{-1}\mathbf{A}_{12})^{-1}$, we have

$$\begin{aligned}\mathbf{G}(s)&=-\frac{1}{L_\mathrm{f}}\mathbf{A}_{11}^{-1}\mathbf{A}_{12}\mathbf{X}^{-1}\\&=\frac{1}{D(s)}\begin{bmatrix} b_2\ s^2+b_1 s+b_0 & c_1 s+c_0 \\ -(c_1 s+c_0) & b_2\ s^2+b_1 s+b_0 \end{bmatrix}\end{aligned} \tag{20}$$

where $D(s)=a_4\ s^4+a_3\ s^3+a_2\ s^2+a_1 s+a_0$, $a_4=L_\mathrm{f}^2C_\mathrm{f}^2$, $a_3=2R_\mathrm{f}L_\mathrm{f}C_\mathrm{f}^2$, $a_2=R_\mathrm{f}^2C_\mathrm{f}^2+2L_\mathrm{f}^2C_\mathrm{f}^2\omega_0^2+2L_\mathrm{f}C_\mathrm{f}$, $a_1=2R_\mathrm{f}L_\mathrm{f}C_\mathrm{f}^2\omega_0^2+2R_\mathrm{f}C_\mathrm{f}$, $a_0=R_\mathrm{f}^2C_\mathrm{f}^2\omega_0^2+L_\mathrm{f}^2C_\mathrm{f}^2\omega_0^4-2L_\mathrm{f}C_\mathrm{f}\omega_0^2+1$, $b_2=L_\mathrm{f}C_\mathrm{f}$, $b_1=R_\mathrm{f}C_\mathrm{f}$, $b_0=1-L_\mathrm{f}C_\mathrm{f}\omega_0^2$, $c_1=2L_\mathrm{f}C_\mathrm{f}\omega_0$, and $c_0=R_\mathrm{f}C_\mathrm{f}\omega_0$. The Smith–McMillan form can be utilized to determine the poles and zeros of a MIMO system's matrix transfer function [28]. Let $\boldsymbol{\mathcal{M}}(s)$ stands for the Smith–McMillan form of $\mathbf{G}(s)$ in (20). To compute $\boldsymbol{\mathcal{M}}(s)$, the matrix transfer function is expressed as $\mathbf{G}(s)=\mathbf{P}(s)/D(s)$, where $D(s)$ is a polynomial that is the least common multiple of the denominators of all the elements of $\mathbf{G}(s)$, and $\mathbf{P}(s)$ is a polynomial matrix. The Smith form of $\mathbf{P}(s)$ is given as follows [28]:

$$\mathbf{S}(s)=\begin{bmatrix} \epsilon_1(s) & 0 \\ 0 & \epsilon_2(s) \end{bmatrix} \tag{21}$$

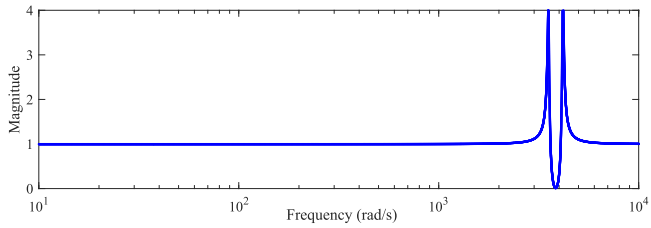

Fig. 3. $\lambda(j\omega)$ of the open-loop system.

where $\epsilon_1(s)$ and $\epsilon_2(s)$ are two polynomials computed as

$$\epsilon_\mathrm{i}(s)=\frac{Q_\mathrm{i}(s)}{Q_{\mathrm{i}-1}(s)},\qquad i=1,2 \tag{22}$$

where $Q_0(s)=1$, and $Q_\mathrm{i}(s)$ is the greatest common divisor of all $(i\times i)$ minors of $\mathbf{P}(s)$. According to (20), the greatest common divisor of all (1×1) minors of $\mathbf{P}(s)$ is 1, and the greatest common divisor of (2×2) minors of $\mathbf{P}(s)$ is $D(s)$. Therefore, the Smith form of $\mathbf{P}(s)$ is

$$\mathbf{S}(s)=\begin{bmatrix} 1 & 0 \\ 0 & D(s) \end{bmatrix}. \tag{23}$$

Consequently, the Smith–McMillan form of $\mathbf{G}(s)$ is given as follows:

$$\boldsymbol{\mathcal{M}}(s)=\begin{bmatrix} \frac{1}{D(s)} & 0 \\ 0 & 1 \end{bmatrix}. \tag{24}$$

Using (24), the open-loop system has four poles in the left-half plane without any zeros; and thus, the system is minimum phase. Since the DER is a MIMO system with two control loops, it is necessary to assess the intensity of interactions between these control loops. To this end, the relative gain array (RGA) matrix, as a commonly used tool, is utilized. The RGA matrix of a nonsingular square matrix $\mathbf{G}(j\omega)$ is defined as

$$\boldsymbol{\Lambda}(\omega)=\mathbf{G}(j\omega)\odot\mathbf{G}^*(j\omega) \tag{25}$$

where $\odot$ and $*$ represent the elementwise Hadamard product and the transpose of the inverse matrix, respectively [28]. Using (25), the RGA matrix of (20) in the steady state is computed at $\omega=0$ as follows:

$$\boldsymbol{\Lambda}(0)=\begin{bmatrix} \lambda & 1-\lambda \\ 1-\lambda & \lambda \end{bmatrix},\quad \lambda=\frac{1}{1+\left(\frac{R_\mathrm{f}C_\mathrm{f}\omega_0}{1-L_\mathrm{f}C_\mathrm{f}\omega_0^2}\right)^2}. \tag{26}$$

Since in practice $R_\mathrm{f}C_\mathrm{f}\omega_0\ll 1-L_\mathrm{f}C_\mathrm{f}\omega_0^2$, the steady-state RGA matrix is almost diagonal; and therefore, there is no considerable interactions between the control loops in low frequencies. Nevertheless, in high frequencies, the same analysis shows that the interactions between the control loops are considerable. To graphically investigate this fact, Fig. 3 shows the plot of $\lambda(j\omega)$ of the open-loop system over the desired frequency range of the system for $L_\mathrm{f}=1.35$ mH, $C_\mathrm{f}=50$ μF, and $R_\mathrm{f}=0.1$ Ω. As can be seen from Fig. 3, since $\lambda(j\omega)$ is not close to 1, the RGA matrix is not close to the identity matrix; and thus, the interactions between the control loops are not negligible. Hence,

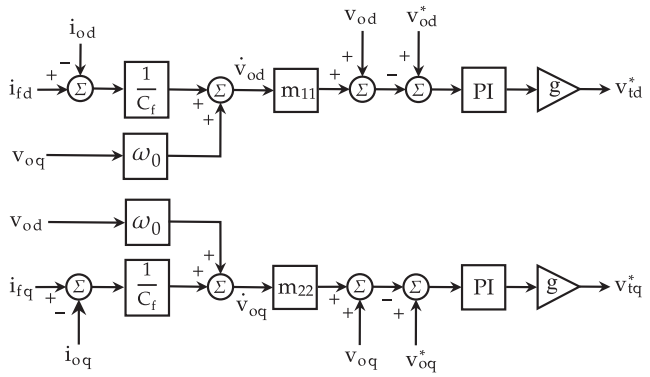

Fig. 4. Structure of the high-gain MIMO PI controller.

in the conventional control techniques, where the control laws for $v_{\rm td}$ and $v_{\rm tq}$ are independently designed by dividing the system into two single-input single-output subsystems, the performance of the system is degraded in the transient. In the following, to tackle this problem, a MIMO technique is proposed to design a unified controller for the system. The proposed controller is designed according to Algorithm 1.

1) *Step 1:* Since $\mathbf{CB}$ is not full rank, a new extended output $w(t)$ should be defined as given by (3). The measurement matrix $\mathbf{M} = [m_{ij}]$ $(i, j = 1, 2)$ must be selected such that $\mathbf{F}_2$ is full rank. Based on (2) and (3), $\mathbf{F}_2$ is computed as

$$\mathbf{F}_2 = \mathbf{C}_2 + \mathbf{M}\begin{bmatrix} \frac{1}{C_f} & 0 \\ 0 & \frac{1}{C_f} \end{bmatrix} = \frac{1}{C_f}\begin{bmatrix} m_{11} & m_{12} \\ m_{21} & m_{22} \end{bmatrix}. \quad (27)$$

By selecting $m_{11} = m_{22} = \tau > 0$ and $m_{12} = m_{21} = 0$, $\mathbf{F}_2$ is full rank. Therefore, using (3), $\mathbf{F}_1$ is given as follows:

$$\mathbf{F}_1 = \mathbf{C}_1 + \mathbf{M}\begin{bmatrix} 0 & \omega_0 \\ -\omega_0 & 0 \end{bmatrix} = \begin{bmatrix} 1 & \tau\omega_0 \\ -\tau\omega_0 & 1 \end{bmatrix}. \quad (28)$$

The second category of the slow poles ($|\lambda\mathbf{I}_m - \mathbf{A}_{11} + \mathbf{A}_{12}\mathbf{F}_2^{-1}\mathbf{F}_1| = \mathbf{0}$) is placed in $-1/\tau < 0$.

2) *Step 2:* $\sigma_1 = \sigma_2 = \sigma > 0$ is considered.

3) *Step 3:* The controller gain $\mathbf{K}_{\rm P}$ is calculated as follows:

$$\mathbf{K}_P = (\mathbf{B}_2\mathbf{F}_2)^{-1}\mathbf{\Sigma} = C_f L_f \begin{bmatrix} \frac{\sigma}{\tau} & 0 \\ 0 & \frac{\sigma}{\tau} \end{bmatrix}. \quad (29)$$

4) *Steps 4 and 5:* The controller gain $\mathbf{K}_{\rm I}$ is computed as $\mathbf{K}_I = \alpha\mathbf{K}_P$. α and g will be selected later.

Fig. 4 shows the block diagram of the proposed high-gain MIMO PI controller. As can be seen from this figure, not only is the PCC voltage used to construct the tracking error but also the inverter output current and the load current are utilized. Therefore, in addition to regulating the PCC voltage, this MIMO controller can eliminate the adverse effects of circulating currents caused by nonlinear/unbalanced loads. Since $\mathbf{C}_2 = \mathbf{0}_{2\times 2}$, according to (8)–(13), the fast dynamics and the first categories of slow dynamics are not observable. These dynamics, known as the internal system dynamics, have no effects on the output response. Nevertheless, to achieve a stable closed-loop system, these internal dynamics must be stabilized by placing their corresponding states in the open left half of the complex plane. Using (27)–(29) in (8) and when g tends to infinity, the following ideal closed-loop transfer function is obtained:

$$\begin{bmatrix} v_{\rm od} \\ v_{\rm oq} \end{bmatrix} = \begin{bmatrix} \frac{1}{\tau s+1} & 0 \\ 0 & \frac{1}{\tau s+1} \end{bmatrix}\begin{bmatrix} v_{\rm odref} \\ v_{\rm oqref} \end{bmatrix} = \mathbf{T}_\infty(s)\begin{bmatrix} v_{\rm odref} \\ v_{\rm oqref} \end{bmatrix}. \quad (30)$$

To complete the controller design, parameters τ, α, and σ should be selected to achieve the desired performance. According to (30), τ can be defined as the ideal time constant of the closed-loop system. To select this parameter, two issues should be taken into account. First, the small values of τ lead to fast responses, which are desirable. Second, as the BW of the closed-loop system, which equals $1/\tau$, should be small, for example ten times smaller than the switching frequency of the inverters, larger values of τ are of our interest. To make a tradeoff and depending on the requirements of the application and the switching frequency of the inverters, τ is commonly selected between 0.5 and 5 ms [27]. The poles connected with the internal dynamics of the closed-loop system are located at $-\alpha$ and $-\sigma g$. These poles must be sufficiently far from the imaginary axis so that the internal dynamics quickly tends to zero. As mentioned earlier, (8) and (9) are valid when g tends to infinity. On the other hand, g has a direct effect on the amplitude of the control signals. A relatively large value for g maintains the system performance where its price is computing control signals with large amplitudes. Therefore, g is used to make a compromise between the amplitude of the control signals and the modeling error. To numerically follow the design procedure, consider a DER with $L_{\rm f} = 1.35$ mH, $C_{\rm f} = 50$ μF, and $R_{\rm f} = 0.1$ Ω. τ is set to 0.5 ms for a fast response; α and σ are set to 1000 and 1, respectively. If $g \to \infty$, the poles associated with the internal dynamics of the closed-loop system are located at -1000, -1000, $-\infty$, and $-\infty$; and the controllable and observable subsystem (30) has two poles both located at -2000. With these parameters, the controller gains are as follows:

$$\mathbf{K}_{\rm I} = 1000\mathbf{K}_{\rm P} = \begin{bmatrix} 0.135 & 0 \\ 0 & 0.135 \end{bmatrix}. \quad (31)$$

To select the value of g, in Table I, the poles of the controllable and observable subsystem (30) are reported for three limited values of this parameter. For a given value of g, the corresponding desired closed-loop system is shown with $\mathbf{T}_g(s)$. In Table I, the error $e = \|\mathbf{T}_g(s) - \mathbf{T}_\infty(s)\|_\infty$ is also listed where $\|.\|_\infty$ is the infinite norm. As expected, by increasing g, the poles approach $-1/\tau$ and e decreases. In Fig. 5(a), the upper ($\bar{\sigma}$) and lower ($\underline{\sigma}$) bounds of the singular values of $\mathbf{T}_g(s)$ are depicted. Furthermore, the response of the desired closed-loop system is shown in Fig. 5(b), where step changes are considered

TABLE I
EFFECTS OF g ON THE DESIRED CLOSED-LOOP SYSTEM

g	10^4	5×10^4	10^5
Eigenvalues	$-500 \pm j4.1$	$-797 \pm j4$	$-879 \pm j3$
	$-4387 \pm j3843$	$-2692 \pm j54$	$-2149 \pm j15$
	$-5185 \pm j4467$	$-46585 \pm j678$	$-96846 \pm j650$
e	0.277	0.0718	0.0372

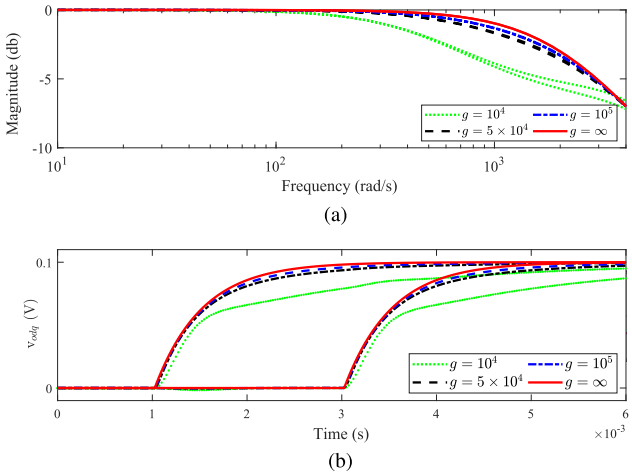

Fig. 5. Effects of g on the desired closed-loop system. (a) Upper ($\bar{\sigma}$) and lower ($\underline{\sigma}$) bounds of the singular values. (b) Step response of the desired closed-loop system.

TABLE II
SPECIFICATIONS OF THE DERS TEST SYSTEM

Parameter	Description	Case 1	Case 2	Case 3
$V_{\rm DC}$	DC link voltage	680 V	2000 V	650 V
$V_{\rm MG}$	VSC terminal voltage	311 V	630 V	325 V
f	Nominal frequency	50 Hz	60 Hz	50 Hz
$C_{\rm f}$	Capacitance of LCL filter	50 μF	500 μF	25 μF
$L_{\rm f}$	Input inductance of LCL filter	1.35 mH	0.3 mH	1.8 mH
$R_{\rm f}$	Input resistance LCL filter	100 mΩ	3 mΩ	100 mΩ
$L_{\rm c}$	Output inductance of LCL filter	0.35 mH	0.3 mH	1.8 mH
$R_{\rm c}$	Output resistance of LCL filter	30 mΩ	3 mΩ	100 mΩ

as the reference set points of $v_{\rm odref}$ and $v_{\rm oqref}$ at $t = 1$ s and $t = 3$ s, respectively. All these considered, in the rest of this article, $g = 10^5$ is selected for the designed high-gain MIMO PI controller since e is small enough for this value. The design procedure of the high-gain MIMO PI controllers is illustrated in the flowchart, as presented in Fig. 6. In this figure, $\mathfrak{Re}\{\lambda_s\}$ stands for the real parts of the eigenvalues of $\mathbf{A}_{11} - \mathbf{A}_{12}\mathbf{F}_2^{-1}\mathbf{F}_1$.

IV. SIMULATION RESULTS

In this section, the designed high-gain robust MIMO PI controller is implemented on inverter-based DERs.

A. Comparison Results

In this scenario, the performance of the proposed controller is compared with those of a conventional controller [29], a robust H_2/H_∞ controller [10], and an optimal controller [9]. The tested system is a DER that can operate in both grid-connected and islanded modes, as shown in Fig. 7. Since the DERs in [4], [9], [10] are different, in each comparison, the proposed high-gain MIMO PI controller is redesigned based on the parameters of the case studies, as reported in Table II. The DERs are connected to the main grid that supports the voltage and frequency control. It is assumed that the DERs are disconnected from the main grid at $t = 0.05$ s and placed in the islanded mode. At $t = 0.08$ s, the same active power changes occur, and since the active power

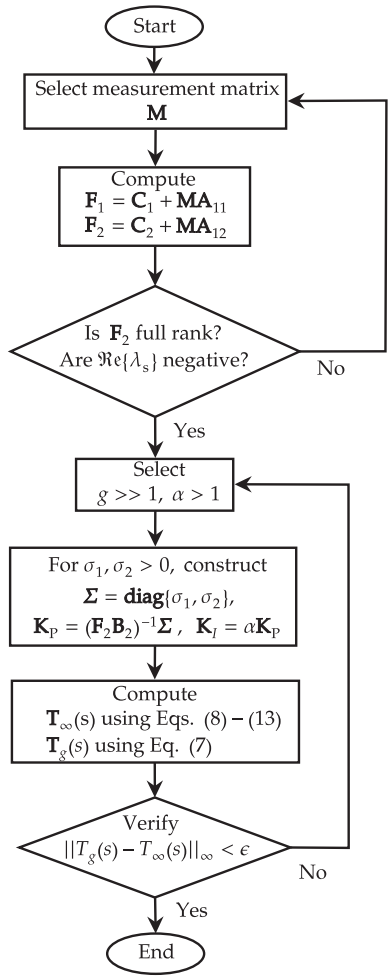

Fig. 6. Flowchart of the high-gain MIMO PI controller design.

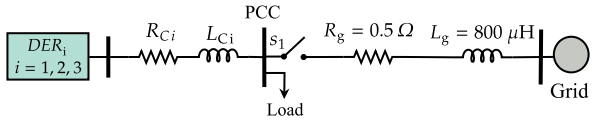

Fig. 7. Block diagram of the system in mode transition and load variations.

changes do not affect the reference voltage, the PCC voltage must return to its nominal value.

1) Conventional PI Controller: For a DER with parameters reported in Table II, Case 1, Fig. 8 shows the performance of the proposed controller and a conventional PI controller tuned by the method presented in [4]. According to Fig. 8(a), when the operating mode of the system is changed from the grid connected to the islanded mode, the voltage of the PCC is smoothly transferred to the new stable set point. This state transition occurs in less than 4 ms with the proposed controller, whereas it takes around 8 ms with the conventional PI controller. In the event of the islanded operation, when changes in the active power disturb the PCC voltage, the proposed controller can reject this disturbance in the first oscillation, while the conventional PI controller rejects it after six oscillations. As can be seen from Fig. 8(a), in the proposed technique, the disturbance effects

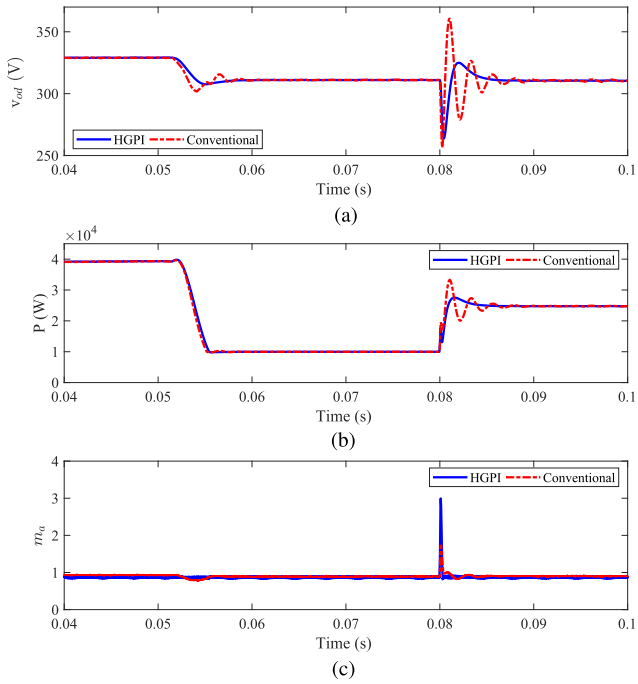

Fig. 8. Proposed HGPI controller versus conventional PI controller: transition from the grid-connected mode to the island mode, and three-phase active power changes. (a) Output voltage (*d*-axis). (b) Output active power. (c) Modulating index.

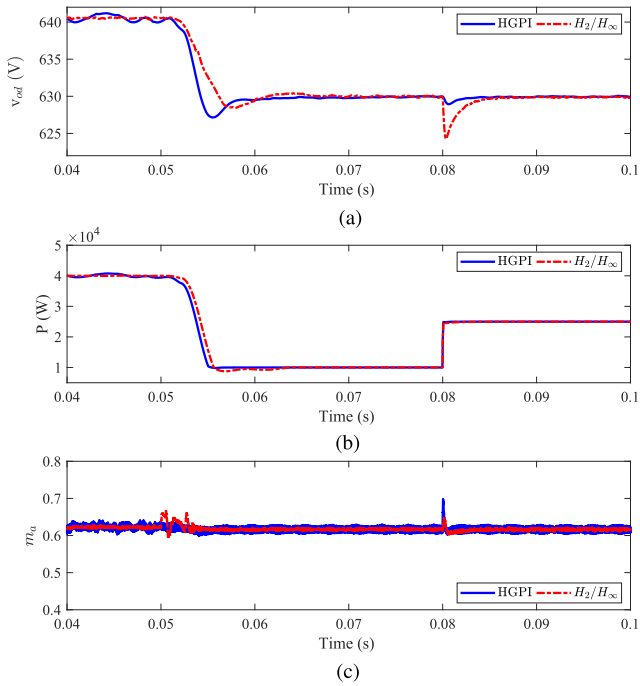

Fig. 9. Proposed HGPI controller versus H_2/H_∞ controller: transition from the grid-connected mode to the island mode, and three-phase active power changes. (a) Output voltage (*d*-axis). (b) Output active power. (c) Modulating index.

are in the range of $[-14\%, 4.5\%]$, whereas in the conventional method, it is in the range of $[-19\%, 17.5\%]$. In addition, the developed control approach can track the active power reference with a maximum overshoot of 12% and a settling time of 2 ms. However, the conventional method leads to a 36% overshoot and 10 ms settling time, as observed in Fig. 8(b).

2) Robust H_2/H_∞ Controller: The performance of the suggested controller and a robust H_2/H_∞ controller, which was designed using the technique described in [10] for a DER with parameters in Table II-Case 2, is shown in Fig. 9. In both the control techniques, the PCC voltage is transferred to its new stable set point in the same amount of time, as can be seen in Fig. 9(a). In the islanded mode, nevertheless, the disturbance caused by changes in the active power in the PCC voltage is eliminated after about 4 ms and 10 ms by the suggested control method and the H_2/H_∞ controller, respectively. Moreover, the amplitude of the disturbance caused by these load changes is 0.09% and 1.7%, respectively.

3) Optimal Linear Quadratic Tracking (LQT) Controller: Fig. 10 depicts the performance of the proposed controller and the LQT controller for a DER with parameters in Table II-Case 3 [9]. According to Fig. 10(a), although the performance of the LQT controller is not proper during the transition from the connection mode, it seems that this controller outperforms the proposed controller in the islanded mode. Nevertheless, since the LQT controller does have any integrators in its structure, this controller is unable to eliminate the steady-state error, whereas the high-gain MIMO PI controller accomplishes this crucial goal. Due to the scale of the plot, this steady-state error in the LQT response cannot be recognized in the *d*-axis voltage tracking, but it can be easily detected in the *q*-axis voltage tracking, as shown in Fig. 10(b). The analysis of the switching modulation index, as an index of the control effort shown with m_a, can indicate an additional advantage of the suggested control approach over the LQT controller. Fig. 10(d) shows that, in the suggested method, the stable value of the switching modulation index is always less than one, while for the LQT controller, this value becomes greater than one. For $|m_a| > 1$, the modulation process is referred to as overmodulation, and this phenomenon can cause the appearance of low-order harmonics in the ac voltage spectrum [27], [30].

According to the above results and paying attention to some important advantages of the proposed high-gain MIMO PI controller, such as providing extra flexibility in the design of the outer control layer (secondary layer) due to its simple first-order closed-loop transfer function, it can be inferred that the proposed controller ranks first among the studied controllers.

B. Plug-and-Play Capability

As mentioned earlier, one of the primary control responsibilities is to enable the plug-and-play capability for DERs. While it is usually needed to establish specific control algorithms to achieve this capability, the proposed high-gain MIMO PI controller can address this issue without any additional control algorithms. This self-synchronization property of the suggested controller is investigated by assuming that S_1 is open and S_2 is closed at $t = 0.4$ s when significant differences in the phases and amplitudes of the DERs are observed. As shown in Figs. 11 and 12, when S_2 is closed, after two cycles, the voltage of

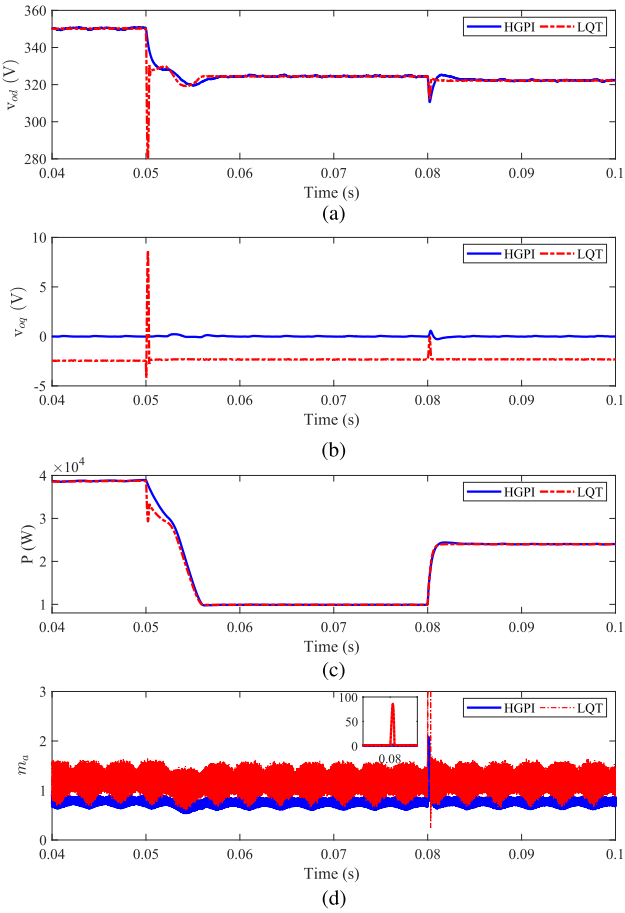

Fig. 10. Proposed HGPI controller versus LQT controller: transition from the grid-connected mode to the island mode, and three-phase active power changes. (a) and (b) Output voltage (*dq*-axis). (c) Output active power. (d) Modulating index.

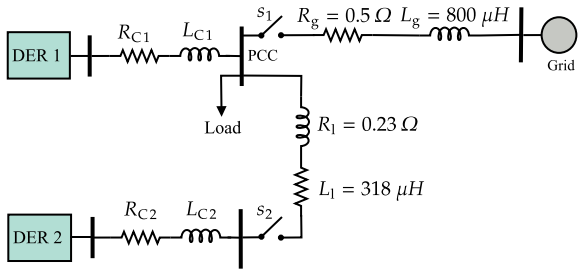

Fig. 11. Studied of island and grid-connected mode as well as plug-and-play capability of DERs.

the DERs has the same amplitude and phase, and in the new stable equilibrium point, they feed the 40 kW load with a power factor of 0.8. Thus, the high-gain robust MIMO PI controller can maintain its performance even in this challenging situation.

C. Islanded Microgrid

In this scenario, the designed high-gain MIMO PI controller is applied to a microgrid that consists of four DERs, as shown in Fig. 13. For the first and second loads, increasing and decreasing changes in the demand load are taken into account, as

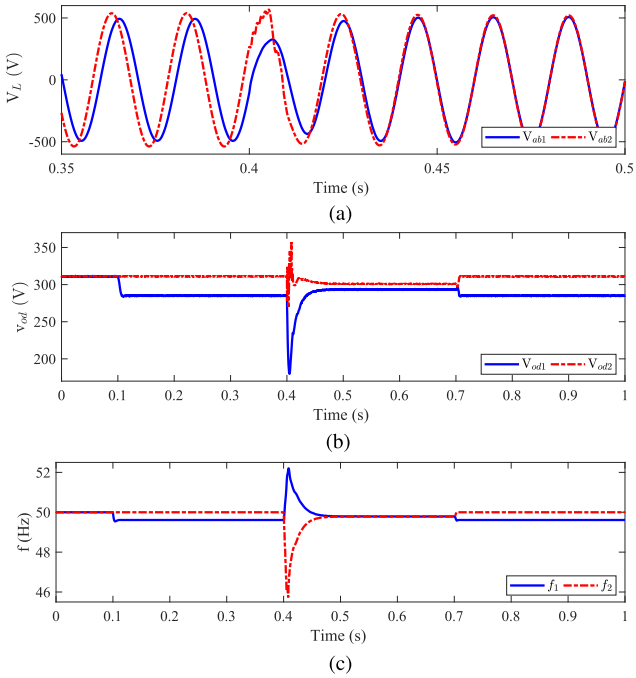

Fig. 12. Plug-and-play capability. (a) Output line voltage (*abc*-frame). (b) Output voltage (*d*-axis). (c) Frequency.

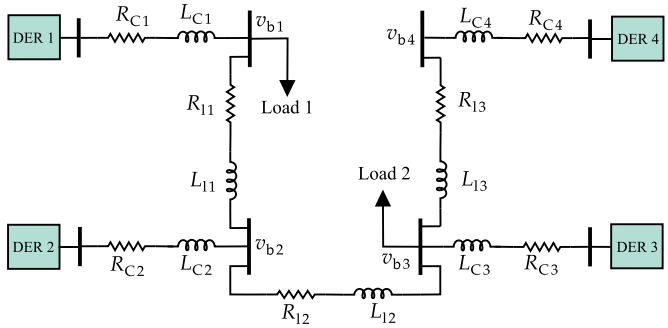

Fig. 13. Studied four DERs islanded microgrid.

summarized in Table III [29]. To investigate the ability of the closed-loop system to track the desired reference signals, which are provided by the droop control, Fig. 14(a) shows the voltages of all the DERs. The proposed high-gain MIMO PI controller performs satisfying results, although the secondary voltage and frequency controllers are not activated in the control system. Fig. 14(b) shows the frequency of each DER where the designed controllers are able to maintain the frequencies in acceptable ranges. The active power is shown in Fig. 14(c), where the DERs are equipped with the MIMO robust controllers. As seen from these figures, the control scheme successfully shares the active power among the DERs.

V. Experimental Results

The performance of the proposed controller is investigated using a laboratory experiment with the parameters, as presented in Table III, DER 1. The experimental circuit, that is able to operate in either islanded mode or grid-connected mode, consists

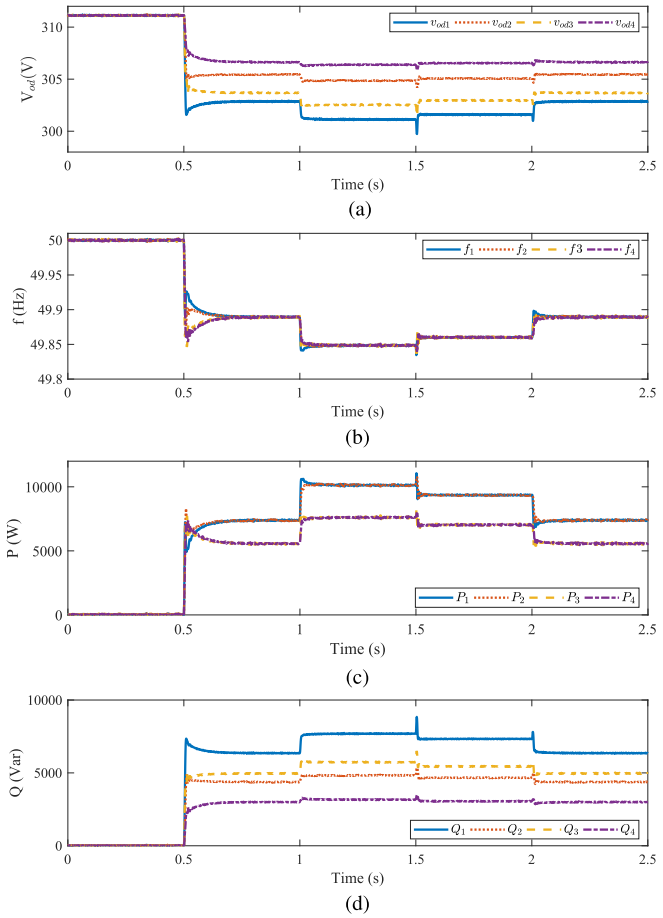

Fig. 14. Proposed controller in islanded microgrid: effects of three-phase load changes. (a) Output voltage (d-axis). (b) Frequency. (c) Output active power changes. (d) Output reactive power changes.

TABLE III
SPECIFICATIONS OF THE MICROGRID TEST SYSTEM

Parameter	Description	DER 1 and 2	DER 3 and 4
S	VSC rated power	45 kVA	34 kVA
$V_{\rm DC}$	DC-link voltage	680 V	680 V
$V_{\rm MG}$	VSC terminal voltage	311 V	311 V
f	Nominal frequency	50 Hz	50 Hz
$m_{\rm p}$	P-ω droop coefficient	9.4×10^{-5}	12.5×10^{-5}
$m_{\rm q}$	Q–E droop coefficient	1.3×10^{-3}	1.5×10^{-3}
$C_{\rm f}$	Capacitance of LCL filter	50 μF	50 μF
$L_{\rm f}$	Input inductance of LCL filter	1.35 mH	1.35 mH
$R_{\rm f}$	Input resistance of LCL filter	0.1 Ω	0.1 Ω
$L_{\rm c}$	Output inductance of LCL filter	0.35 mH	0.35 mH
$R_{\rm c}$	Output resistance of LCL filter	0.03 Ω	0.03 Ω
Line impedance			
	Line 1	$R_{l1} = 0.23\ \Omega$	$L_{l1} = 318\ \mu$H
	Line 2	$R_{l2} = 0.35\ \Omega$	$L_{l2} = 1847\ \mu$H
	Line 3	$R_{l3} = 0.23\ \Omega$	$L_{l3} = 318\ \mu$H
Load changes (VA)			
Time	$0.5 < t < 1$	$1 < t < 1.5$	$1.5 < t < 2$	$2 < t < 2.5$
Load 1	$12000 + j12000$	$18000 + j13500$	$16500 + j13000$	$12000 + j12000$
Load 2	$15300 + j7600$	$19800 + j9100$	$18300 + j8600$	$15300 + j7600$

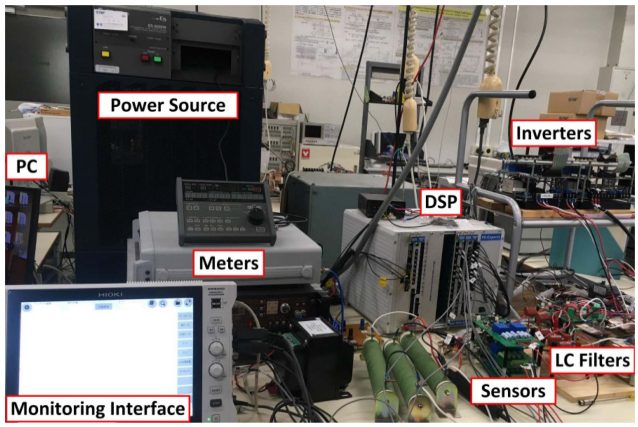

Fig. 15. Schematic diagram of the experimental setup.

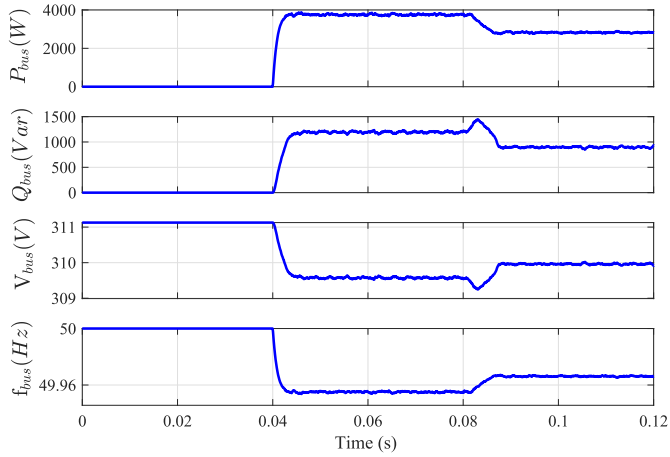

Fig. 16. Experimental results in the islanded operation mode.

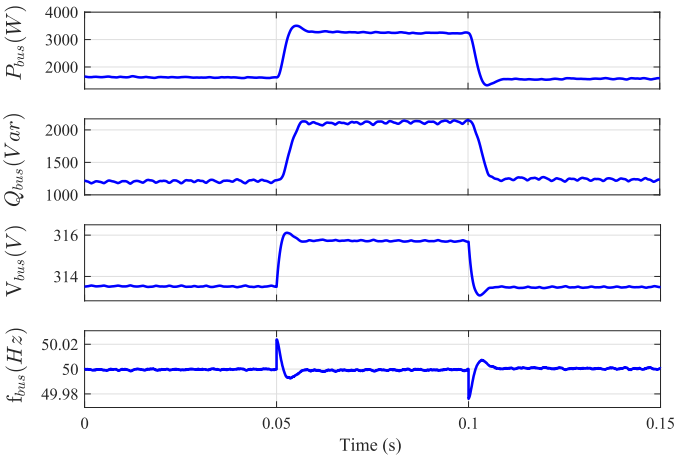

Fig. 17. Experimental results in the grid-connected mode.

of an inverter-based DER system, as shown in Fig. 7. The laboratory setup is illustrated in Fig. 15. The inverter is controlled by a digital signal processor system Myway Plus PE-Expert4, and the measurements are gathered using the "Wave" function of this system, which transfers the real-time values from the controller to the interfaced PC. In the islanded operation mode, a step change in the active and reactive loads is taken into account when a 4000 VA load with a power factor of 0.95 ($\Delta P_{\rm Load} = 3800$ W and $\Delta Q_{\rm Load} = 1270$ Var) is delivered to the system at $t = 0.04$ s, and a quarter of the system's load is removed ($\Delta P_{\rm Load} = -950$ W and $\Delta Q_{\rm Load} = -317$ Var) at

$t = 0.08$ s, as shown in Fig. 16. Since the voltage and frequency references are defined by the droop control, the PCC voltage and frequency shift proportionally to the coefficients of the active power and reactive power droops, and the system states become stable at a new equilibrium point.

In the grid-connected mode, the performance of the system is investigated when the reference power changes as $\Delta P_{\text{ref}} = \pm 1600$ W, and $\Delta Q_{\text{ref}} = \pm 1000$ Var between $t = 0.05$ s and $t = 0.1$ s, as shown in Fig. 17. In this mode of operation, the voltage and frequency references are imposed by the main grid. As can be seen in Fig. 17, the proposed robust PI controller leads to a smooth transition in the voltage and active/reactive power at the load bus.

VI. Conclusion

In this article, high-gain robust MIMO PI controllers are designed to control the voltage of ac microgrids. The parameters of the controllers are tuned based on the first Markov parameter of the microgrids; and therefore, it has been independent of the state matrix of the system. Unlike other robust control techniques that lead to high-order closed-loop systems, the suggested MIMO PI method has a fixed-order structure. Moreover, it has a unified structure where the current and voltage are simultaneously regulated. The proposed controller can address the problem of current saturation in a direct way, i.e., without employing any individual current limiters. Since the designed MIMO controller is robust against uncertainty and external disturbances, the obtained closed-loop system maintains its stability and shows acceptable performance even in conditions, such as large disturbances. The closed-loop system has a first-order transfer function with stable internal dynamics. As a result, the control configuration is straightforward to examine at the zero-level layer and can be utilized to design controllers for the higher levels. The simulation results have indicated that the designed high-gain MIMO PI controller can successfully improve the performance of the voltage control in microgrids.

References

[1] R. Heydari, T. Dragicevic, and F. Blaabjerg, "High-bandwidth secondary voltage and frequency control of VSC-based AC microgrid," *IEEE Trans. Power Electron.*, vol. 34, no. 11, pp. 11320–11331, Nov. 2019.

[2] H. Bevrani, A. Ghosh, and G. Ledwich, "Renewable energy sources and frequency regulation: Survey and new perspectives," *IET Renewable Power Gener.*, vol. 4, no. 5, pp. 438–457, Sep. 2010.

[3] D. E. Olivares et al., "Trends in microgrid control," *IEEE Trans. Smart Grid*, vol. 5, no. 4, pp. 1905–1919, Jul. 2014.

[4] A. Bidram, A. Davoudi, F. L. Lewis, and J. M. Guerrero, "Distributed cooperative secondary control of microgrids using feedback linearization," *IEEE Trans. Power Syst.*, vol. 28, no. 3, pp. 3462–3470, Aug. 2013.

[5] A. Mehrizi-Sani and R. Iravani, "Potential-function based control of a microgrid in islanded and grid-connected modes," *IEEE Trans. Power Syst.*, vol. 25, no. 4, pp. 1883–1891, Nov. 2010.

[6] T. Dragičević, "Model predictive control of power converters for robust and fast operation of AC microgrids," *IEEE Trans. Power Electron.*, vol. 33, no. 7, pp. 6304–6317, Jul. 2018.

[7] X. Guo, Z. Lu, B. Wang, X. Sun, L. Wang, and J. M. Guerrero, "Dynamic phasors-based modeling and stability analysis of droop-controlled inverters for microgrid applications," *IEEE Trans. Smart Grid*, vol. 5, no. 6, pp. 2980–2987, Nov. 2014.

[8] Z. Zhang et al., "Advances and opportunities in the model predictive control of microgrids: Part I–primary layer," *Int. J. Elect. Power Energy Syst.*, vol. 134, 2022, Art. no. 107411.

[9] Y. Batmani, Y. Khayat, S. Najafi, and J. M. Guerrero, "Optimal integrated inner controller design in AC microgrids," *IEEE Trans. Power Electron.*, vol. 37, no. 9, pp. 10372–10383, Sep. 2022.

[10] S. Gholami, S. Saha, and M. Aldeen, "Robust multiobjective control method for power sharing among distributed energy resources in islanded microgrids with unbalanced and nonlinear loads," *Int. J. Elect. Power Energy Syst.*, vol. 94, pp. 321–338, Jan. 2018.

[11] A. Saleh, A. Deihimi, and R. Iravani, "Model predictive control of distributed generations with feed-forward output currents," *IEEE Trans. Smart Grid*, vol. 10, no. 2, pp. 1488–1500, Mar. 2019.

[12] R. Pérez-Ibacache, A. L. Cedeño, C. A. Silva, G. Carvajal, J. C. Agüero, and A. Yazdani, "Decentralized model-based predictive control for DER units integration in AC microgrids subject to operational and safety constraints," *IEEE Trans. Power Del.*, vol. 36, no. 4, pp. 2479–2489, Aug. 2021.

[13] A. J. Babqi and A. H. Etemadi, "MPC-based microgrid control with supplementary fault current limitation and smooth transition mechanisms," *IET Gener., Transmiss. Distrib.*, vol. 11, no. 9, pp. 2164–2172, Jun. 2017.

[14] O. Babayomi, Y. Li, Z. Zhang, R. Kennel, and J. Kang, "Overview of model predictive control of converters for islanded ac microgrids," in *Proc. IEEE 9th Int. Power Electron. Motion Control Conf.*, 2020, pp. 1023–1028.

[15] S. K. Sarkar, M. H. K. Roni, D. Datta, S. K. Das, and H. R. Pota, "Improved design of high-performance controller for voltage control of islanded microgrid," *IEEE Syst. J.*, vol. 13, no. 2, pp. 1786–1795, Jun. 2019.

[16] M. Shafiee-Rad, Q. Shafiee, M. S. Sadabadi, and M. R. Jahed-Motlagh, "Decentralized voltage stabilization and robust performance satisfaction of islanded inverter-interfaced microgrids," *IEEE Syst. J.*, vol. 15, no. 2, pp. 1893–1904, Jun. 2021.

[17] M. Raeispour, H. Atrianfar, H. R. Baghaee, and G. B. Gharehpetian, "Robust sliding mode and mixed H_2/H_∞ output feedback primary control of ac microgrids," *IEEE Syst. J.*, vol. 15, no. 2, pp. 2420–2431, Jun. 2021.

[18] M. Garcia-Sanz, *Robust Control Engineering: Practical QFT Solutions*. Boca Raton, FL, USA:CRC Press, 2017.

[19] A. Rafiee, Y. Batmani, H. Bevrani, and T. Kato, "Robust MIMO controller design for VSC-based microgrids: Sequential loop closing concept and quantitative feedback theory," *IEEE Trans. Smart Grid*, vol. 13, no. 1, pp. 129–138, Jan. 2022.

[20] H. Bevrani, *Robust Power System Frequency Control*, vol. 4. Berlin, Germany:Springer, 2014.

[21] J. F. Patarroyo-Montenegro, F. Andrade, J. M. Guerrero, and J. C. Vasquez, "A linear quadratic regulator with optimal reference tracking for three-phase inverter-based islanded microgrids," *IEEE Trans. Power Electron.*, vol. 36, no. 6, pp. 7112–7122, Jun. 2021.

[22] R. Pérez-Ibacache, C. A. Silva, and A. Yazdani, "Linear state-feedback primary control for enhanced dynamic response of AC microgrids," *IEEE Trans. Smart Grid*, vol. 10, no. 3, pp. 3149–3161, May 2019.

[23] A. Rafiee, Y. Batmani, F. Ahmadi, and H. Bevrani, "Robust load-frequency control in islanded microgrids: Virtual synchronous generator concept and quantitative feedback theory," *IEEE Trans. Power Syst.*, vol. 36, no. 6, pp. 5408–5416, Nov. 2021.

[24] Y. Wan, T. Keviczky, and M. Verhaegen, "Fault estimation filter design with guaranteed stability using Markov parameters," *IEEE Trans. Autom. Control*, vol. 63, no. 4, pp. 1132–1139, Apr. 2018.

[25] D. Ridgely, S. Banda, and J. Silverthorn, "Design and analysis of a multivariable control system for a CCV-typefighter aircraft," in *Proc. 9th Atmos. Flight Mech. Conf.*, 2012, Art. no. 1350.

[26] D. B. Ridgely, S. S. Banda, and J. J. D'Azzo, "Decoupling of high-gain multivariable tracking systems," *J. Guid., Control, Dyn.*, vol. 8, no. 1, pp. 44–49, May 2012.

[27] A. Yazdani and R. Iravani, *Voltage-Sourced Converters in Power Systems: Modeling, Control, and Applications*. Hoboken, NJ, USA:Wiley, 2010.

[28] S. Skogestad and I. Postlethwaite, *Multivariable Feedback Control: Analysis and Design*. Hoboken, NJ, USA:Wiley, 2005.

[29] A. Bidram, V. Nasirian, A. Davoudi, and F. L. Lewis, *Cooperative Synchronization in Distributed Microgrid Control*. Berlin, Germany:Springer, 2017.

[30] N. Mohan, T. M. Undeland, and W. P. Robbins, *Power Electronics: Converters, Applications, and Design*. Hoboken, NJ, USA:Wiley, 2003.

Ali Rafiee received the bachelor's and master's degrees from Azad University, Tehran, Iran, in 2002 and 2012, respectively. He is currently working toward the Ph.D. degree in power systems with the University of Kurdistan, Sanandaj, Iran.

He has been working as a Teacher in technical and vocational high schools since 2002. His research interests include microgrids and power systems analysis and control.

Yazdan Batmani received the B.Sc. degree in biomedical engineering from the University of Isfahan, Isfahan, Iran, in 2006, and the M.Sc. and Ph.D. degrees in control engineering from the K.N. Toosi University of Technology, Tehran, Iran, in 2009 and 2014, respectively.

From 2015to 2019, he was an Assistant Professor with the Department of Electrical Engineering, University of Kurdistan, Sanandaj, Iran, where he is currently an Associate Professor. His current research interests include nonlinear control systems, networked control systems, applications of control theory in biomedical engineering, robotics, microgrids, and power systems.

Ali Mehrizi-Sani (Senior Member, IEEE) received the Ph.D. degree in electrical engineering from the University of Toronto, Toronto, ON, Canada.

He is currently an Associate Professor with Virginia Tech, Blacksburg, VA, USA. He is an Associate Editor for the IEEE TRANSACTIONS ON ENERGY CONVERSION, IEEE POWER ENGINEERING LETTERS, and *IET Generation, Transmission and Distribution*. Dr. Mehrizi-Sani was a recipient of the 2018 IEEE PES Outstanding Young Engineer Award and 2017 IEEE Mac E. Van Valkenburg Early Career Teaching Award among his recognitions.

Toshiji Kato (Life Senior Member, IEEE) was born in Kyoto, Japan. He received the B.E., M.E., and Ph.D. degrees in electrical engineering from Doshisha University, Kyoto, Japan, in 1979, 1981, and 1986, respectively.

Since 1981, he has been with Doshisha University, where he is currently a Professor with the Department of Electrical Engineering. He was a Visiting Scientist with the Institut de recherche d'Hydro-Québec, Varennes, QC, Canada, in 1990, and the Laboratory for Electromagnetic and Electronic Systems, Massachusetts Institute of Technology, Cambridge, MA, USA, from 1990 to 1992. His current research interests include computer analysis and control of power and power electronic systems.

Dr. Kato is a member of the IEE of Japan.

Hassan Bevrani (Fellow, IEEE) received the Ph.D. degree in electrical engineering from Osaka University, Osaka, Japan, in 2004.

He is currently a Professor and the Program Leader of Smart/Micro Grids Research Center with the University of Kurdistan, Sanandaj, Iran. Over the years, he has worked as a Senior Research Fellow and a Visiting Professor with Osaka University, Kumamoto University, Kyushu Institute of Technology, Doshisha University, Nagoya University (Japan), Queensland University of Technology (Australia), Centrale Lille (France), and Technical University of Berlin (Germany). He is the author and coauthor of 9 international books, 15 book chapters, and more than 500 journal/conference papers. His current research interests include smart grid operation and control, power systems stability and optimization, microgrid dynamics and control, and intelligent/robust control applications in power electric industry.